Primordial Radius Gap and Potentially Broad Core Mass Distributions of Super-Earths and Sub-Neptunes

Eve J. Lee [ID][1,2,3] and Nicholas J. Connors[1,4]

[1] *Department of Physics, McGill University, Montréal, Québec, H3A 2T8, Canada*
[2] *McGill Space Institute, McGill University, Montréal, Québec, H3A 2A7, Canada*
[3] *Institute for Research on Exoplanets, Montréal, Québec, Canada*
[4] *School of Computer Science, McGill University, Montréal, Québec, H3A 0E9, Canada*

ABSTRACT

The observed radii distribution of *Kepler* exoplanets reveals two distinct populations: those that are more likely to be terrestrials ($\lesssim 1.7 R_\oplus$) and those that are more likely to be gas-enveloped ($\gtrsim 2 R_\oplus$). There exists a clear gap in the distribution of radii that separates these two kinds of planets. Mass loss processes like photoevaporation by high energy photons from the host star have been proposed as natural mechanisms to carve out this radius valley. These models favor underlying core mass function of sub-Neptunes that is sharply peaked at $\sim$4–8$M_\oplus$ but the radial-velocity follow-up of these small planets hint at a more bottom-heavy mass function. By taking into account the initial gas accretion in gas-poor (but not gas-empty) nebula, we demonstrate that 1) the observed radius valley is a robust feature that is initially carved out at formation during late-time gas accretion; and 2) that it can be reconciled with core mass functions that are broad extending well into sub-Earth regime. The maximally cooled isothermal limit prohibits cores lighter than $\sim$1–2$M_\oplus$ from accreting enough mass to appear gas-enveloped. The rocky-to-enveloped transition established at formation produces a gap in the radius distribution that shifts to smaller radii farther from the star, similar to that observed. For the best agreement with the data, our late-time gas accretion model favors dust-free accretion in hotter disks with cores slightly less dense than the Earth ($\sim$0.8$\rho_\oplus$) drawn from a mass function that is as broad as $dN/dM_{\rm core} \propto M_{\rm core}^{-0.7}$.

1. INTRODUCTION

In galactic and stellar astronomy, the initial mass function of stars is one of the most fundamental quantity that influences the structural and chemical evolution of the interstellar medium and the galaxy on average. Obtaining an analogous mass function for exoplanets is challenging. Sub-Neptunes and super-Earths dominate the population with many of them at orbital periods beyond $\sim$10 days (e.g., Fressin et al. 2013; Petigura et al. 2013; Burke et al. 2015), where we lose sensitivity to measure their masses with e.g., radial velocity surveys (e.g., Weiss & Marcy 2014). Mass measurements using transit timing variations are available for only a handful of planets in multi-planetary systems, being favorable to those near mean motion resonances (e.g., Wu & Lithwick 2013; Hadden & Lithwick 2014).

Corresponding author: Eve J. Lee
evelee@physics.mcgill.ca

Theoretically, Malhotra (2015) derived a log-normal distribution of total mass (i.e., core + envelope mass) function peaked at $\sim$4–10$M_\oplus$ using the observed period ratio distribution and applying the condition for dynamical stability given by Hill spacing. Wu (2019) searched for a log-normal distribution of core masses that best-fits photoevaporation model to the observed distribution of planetary radii. They argued that a mass distribution sharply peaked at $\sim$8$M_\oplus(M_\star/M_\odot)$ was necessary to reproduce the shape of the "radius valley", a gap in the radius distribution at $\sim$1.3–1.6 $R_\oplus$ predicted by mass loss theory (Owen & Wu 2013) and later confirmed by the California-Kepler Survey (Fulton et al. 2017; Fulton & Petigura 2018) and asteroseismology (Van Eylen et al. 2018). Rogers & Owen (2020) performed a more sophisticated hierarchical inference analysis fitting photoevaporation model to the observed radius-period distribution and concluded a similarly peaked mass distribution (with the median at $\sim$4$M_\oplus$) is required.

Such high masses are at odds with the radial velocity follow-up of *Kepler* planets which reports peak masses as low as $\sim$1$M_\oplus$ (Weiss & Marcy 2014). Furthermore,

the true radius/mass distribution may be more bottom-heavy than previously thought (Hsu et al. 2019).

In this paper, we assess whether a power-law core mass distribution that extends to the sub-Earth masses is consistent with the observed radius distribution as well as the shape of the gap in the radius-period space. Instead of assuming a distribution of initial envelope mass fraction that is independent of core mass, we calculate the expected envelope mass from nebular accretion in the late stages of disk evolution: a gas-poor environment deemed favorable for preventing runaway gas accretion to ensure the formation of super-Earths and sub-Neptunes (Lee et al. 2014; Lee & Chiang 2016).

Section 2 outlines the basic physical ingredients for gas accretion and photoevaporative mass loss, and the model results are presented in Section 3. We summarize, discuss the implications, and conclude in Section 4.

2. METHODS

2.1. *Underlying core mass distribution*

We begin with the ansatz that the underlying sub-Neptune/super-Earth core mass distribution follows a power-law distribution:

$$\frac{dN}{d\log M_{\rm core}} \propto M_{\rm core}^{1-\xi}, \tag{1}$$

where $M_{\rm core}$ is the mass of the core and we choose $\xi \in [0.7, 1.0, 1.3]$; $\xi = 0.7$ is the best-fit power-law slope to the distribution of peak posterior masses of sub-Neptunes from the radial-velocity follow-up by Marcy et al. (2014). Given that radial velocity measurements are biased against low mass objects, we do not choose ξ lower than 0.7. We note that $\xi = 0.7$ is top-heavy, $\xi = 1.0$ is neutral, and $\xi = 1.3$ is bottom-heavy. We also experimented with exponential distribution in linear and logarithm of $M_{\rm core}$ and found them to provide poor match to the data. The minimum and the maximum core masses are set to $0.01 M_\oplus$ and $20 M_\oplus$, respectively. Figure 1 demonstrates the difference between the assumed power-law mass distributions with respect to the best-fit lognormal distributions presented in literature.

2.2. *Initial envelope mass fraction*

For each core, its initial envelope mass fraction is calculated using the analytic scaling relationship derived by Lee & Chiang (2015) appropriate for gas accretion by cooling (equivalent to Phase II of the core accretion theory, Pollack et al. 1996; see also Ginzburg et al. 2016). We modify the expressions for the weak dependence on the nebular density (Lee & Chiang 2016) and for the expected decrease in the bound radius due to
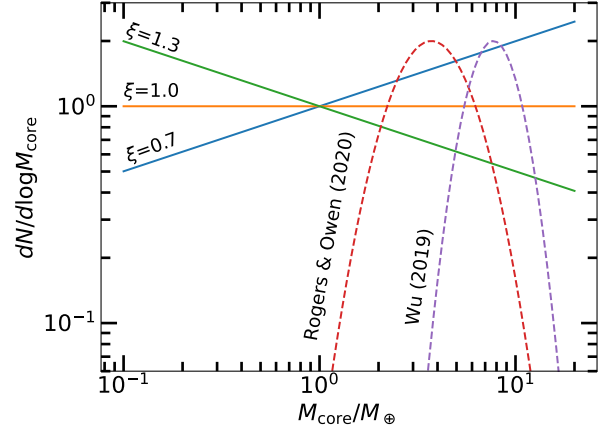

Figure 1. Comparison of power-law core mass distributions used in this paper and best-fit lognormal distributions from Wu (2019) and Rogers & Owen (2020), their Model I. The non-parametric core mass functions favored by Rogers & Owen (2020) are broader but still feature a sharp fall-off at small core masses, unlike smooth power-law distributions explored in this paper. Normalizations are arbitrary and are adjusted for better visualization.

three-dimensional hydrodynamic effects (Lambrechts & Lega 2017; Fung et al. 2019). Shrinking the outer bound radius decreases the rate of accretion in a linear fashion (Lee et al. 2014; see also Ali-Dib et al. 2020 for understanding this effect in terms of entropy delivery). We verified that the expressions we provide here match the numerical calculations.

First, cores need to be sufficiently massive to accrete gas. Their gravitational sphere of influence must encompass the cores themselves so that the speed of gas is below the cores' surface escape speed. We calculate the envelope mass only for cores that satisfy

$$R_{\rm core} \leq R_{\rm out} \equiv f_R \min(R_{\rm Hill}, R_{\rm Bondi})$$

$$M_{\rm core} \geq 0.02 \, M_\oplus \left(\frac{T_{\rm disk}}{1000 \, K}\right)^{4/3}, \tag{2}$$

where $R_{\rm core} \equiv R_\oplus (M_{\rm core}/M_\oplus)^{1/4}$ (Valencia et al. 2006), $R_{\rm out}$ is the outer radius of the bound envelope, $f_R < 1$ is a numerical factor that takes into account the effect of three-dimensional advective flows, $R_{\rm Hill}$ is the Hill radius, $R_{\rm Bondi}$ is the Bondi radius, $T_{\rm disk} = 1000 \, K \, f_T (a/0.1 \, {\rm AU})^{-3/7}$ is the disk temperature, a is the orbital distance, and f_T is a numerical coefficient and a free parameter. We note that for these small cores, $R_{\rm Bondi} < R_{\rm Hill}$ inside 1 AU. We have implicitly assumed a passively heated disk (i.e., heating dominated by stellar irradiation). In Sections 3.1 and 4.1, we will explore the effect of adopting temperature profiles relevant for

active disks (i.e., heating dominated by viscous accretion).

For dusty accretion, the envelope mass fraction

$$\frac{M_{\mathrm{env}}}{M_{\mathrm{core}}} = 0.06\, f_R \left(\frac{M_{\mathrm{core}}}{5\, M_\oplus}\right)^{1.8} \left(\frac{t}{1\,\mathrm{Myrs}}\right)^{0.4}$$
$$\times \left(\frac{\Sigma_{\mathrm{gas}}}{2000\,\mathrm{g\,cm}^{-2}}\right)^{0.12} \left(\frac{0.02}{Z}\right)^{0.4} \left(\frac{\mu}{2.37}\right)^{3.4} \quad (3)$$

where M_{env} is the mass of the gaseous envelope, t is the accretion time, $\Sigma_{\mathrm{gas}} = 1.3 \times 10^5\,\mathrm{g\,cm}^{-2}\, f_{\mathrm{dep}}\, (a/0.2\,\mathrm{AU})^{-1.6}$ is the local disk gas surface density (Chiang & Laughlin 2013), f_{dep} is the disk gas depletion factor, Z is the envelope metallicity, and μ is the envelope mean molecular weight. Similarly, for dust-free accretion,

$$\frac{M_{\mathrm{env}}}{M_{\mathrm{core}}} = 0.25\, f_R \left(\frac{M_{\mathrm{core}}}{5\, M_\oplus}\right)^{1.1} \left(\frac{t}{1\,\mathrm{kyrs}}\right)^{0.4} \left(\frac{200\,\mathrm{K}}{T_{\mathrm{disk}}}\right)^{1.5}$$
$$\times \left(\frac{\Sigma_{\mathrm{gas}}}{4 \times 10^5\,\mathrm{g\,cm}^{-2}}\right)^{0.12} \left(\frac{0.02}{Z}\right)^{0.4} \left(\frac{\mu}{2.37}\right)^{2.2}. \quad (4)$$

We express equation 4 with the disk temperature T_{disk}. More precisely, the relevant temperature is that at the envelope radiative-convective boundary. The outer layers of dust-free envelopes are nearly isothermal so adopting T_{disk} obtains the same answer. We note that equations 3 and 4 have been adjusted for $R_{\mathrm{core}} \propto M_{\mathrm{core}}^{1/4}$ compared to Lee & Chiang (2015) who used $R_{\mathrm{core}} \propto M_{\mathrm{core}}^{1/3}$; this adjustment makes no significant difference in our conclusions.

Throughout this paper, $Z = 0.02$ (solar metallicity), $\mu = 2.37$, and t is drawn from a logarithmically uniform distribution that range 0.01 and 1 Myr, consistent with the late-time formation scenario (Lee & Chiang 2016). The log-uniform distribution is chosen to account for core formation by a series of collisional mergers whose doubling timescales lengthen with time (e.g., Dawson et al. 2015). Motivated by Figure 11 of Fung et al. (2019), we explore $f_R = 0.1$ and 0.2. We choose $f_{\mathrm{dep}} = 0.001$ throughout, prompted by the required level of gas depletion to reproduce the observed peaks in period ratios just outside of first order mean-motion resonances (Choksi & Chiang 2020).

For a given core mass, the maximum possible envelope mass that can be accreted is given by a fully isothermal profile (e.g., Lee & Chiang 2015). No cores are allowed to accrete more than this maximally cooled isothermal mass:

$$M_{\mathrm{iso}} = 4\pi\rho_{\mathrm{disk}} \int_{R_{\mathrm{core}}}^{R_{\mathrm{out}}} r^2 \,\mathrm{Exp}\left[\frac{GM_{\mathrm{core}}}{c_{s,disk}^2}\left(\frac{1}{r} - \frac{1}{R_{\mathrm{out}}}\right)\right] dr, \quad (5)$$

where $\rho_{\mathrm{disk}} \equiv \Sigma_{\mathrm{gas}}\Omega/c_{s,\mathrm{disk}}$ is the local nebular volumetric density, Ω is the Keplerian orbital frequency, $c_{s,\mathrm{disk}} = kT_{\mathrm{disk}}/\mu m_H$ is the local disk sound speed, k is the Boltzmann constant, and m_H is the mass of the hydrogen atom. The nebular mean molecular weight μ is assumed to be the same as that of the envelope.

2.3. Estimating radii

While the masses of sub-Neptunes are dominated by the cores, their radii are largely determined by their envelope mass fraction (Lopez & Fortney 2014). We follow closely the procedure devised by Owen & Wu (2017) in converting envelope mass fractions to radii. Only the essential elements are shown here.

First, we assume that after the disk gas is completely dissipated and planets are laid bare to stellar insolation, their outer layers become isothermal and volumetrically thin ($\sim$6 scale heights above the radiative-convective boundary; Lopez & Fortney 2014). From the density profile given by the inner adiabat

$$\rho(r) \simeq \rho_{\mathrm{rcb}}\left[\nabla_{\mathrm{ad}}\frac{GM_{\mathrm{core}}}{c_s^2}\left(\frac{1}{r} - \frac{1}{R_{\mathrm{rcb}}}\right)\right], \quad (6)$$

the total envelope mass

$$M_{\mathrm{env}} \simeq 4\pi\rho_{\mathrm{rcb}}R_{\mathrm{rcb}}^3\left(\nabla_{\mathrm{ad}}\frac{GM_{\mathrm{core}}}{c_s^2 R_{\mathrm{rcb}}}\right)^{1/(\gamma-1)} I_2, \quad (7)$$

where ρ_{rcb} is the density at the radiative-convective boundary (rcb), $\nabla_{\mathrm{ad}} \equiv (\gamma-1)/\gamma$ is the adiabatic gradient, γ is the adiabatic index of the interior, G is the gravitational constant, $c_s \equiv kT_{\mathrm{eq}}/\mu m_H$ is the sound speed evaluated at the location of the planet, $T_{\mathrm{eq}} \equiv T_{\mathrm{eff},\odot}(R_\odot/a)^{0.5}$ is the equilibrium temperature of the planet, R_{rcb} is the radius at the radiative-convective boundary, and I_2 is the structure integral that follows the form

$$I_n \equiv \int_{R_{\mathrm{core}}/R_{\mathrm{rcb}}}^1 x^n (x^{-1}-1)^{1/(\gamma-1)} dx. \quad (8)$$

To eliminate ρ_{rcb}, we use temperature gradient at the rcb so that

$$\rho_{\mathrm{rcb}} = \frac{64\pi\sigma_{\mathrm{sb}}\mu m_H}{3k\kappa}\nabla_{\mathrm{ad}}\frac{GM_{\mathrm{core}}T_{\mathrm{eq}}^3}{L}, \quad (9)$$

where σ_{sb} is the Stefan-Boltzmann constant, $\kappa \equiv 10^C \rho_{\mathrm{rcb}}^\alpha (k/\mu m_H)^\alpha T_{\mathrm{eq}}^{\alpha+\beta}$ is the opacity at the rcb, and L is the cooling luminosity, which can be written as

$$L \simeq \frac{GM_{\mathrm{core}}M_{\mathrm{env}}}{\tau_{\mathrm{KH}}R_{\mathrm{rcb}}}\frac{I_1}{I_2}, \quad (10)$$

where τ_{KH} is the Kelvin-Helmholtz cooling time of the envelope, and I_1 again follows the structure integral

given by equation 8. We vary $\tau_{KH} \in (100, 300)$ Myrs. The former choice provides a good agreement between the analytically derived planetary radius presented here with the numerically computed thermally evolving sub-Neptunes by Lopez & Fortney (2014) at 100 Myrs. The latter choice agrees well with the numerical solutions of Lopez & Fortney (2014) at 1 Gyrs. Substituting equation 10 into equation 9,

$$\rho_{rcb}^{1+\alpha} = \frac{64\pi\sigma_{sb}\mu m_H}{3k}\nabla_{ad}10^{-C}\left(\frac{\mu m_H}{k}\right)^{\alpha}T_{eq}^{3-\alpha-\beta}\frac{I_2}{I_1}$$
$$\times \frac{\tau_{KH}}{M_{env}}\left(\frac{R_{rcb}}{R_{core}}\right)R_{core}. \quad (11)$$

By re-arranging equation 7, we find another equation for ρ_{rcb}:

$$\rho_{rcb} = \frac{M_{env}}{4\pi}\left(\frac{R_{rcb}}{R_{core}}\right)^{-3+1/(\gamma-1)}R_{core}^{-3+1/(\gamma-1)}$$
$$\times \left(\nabla_{ad}\frac{GM_{core}}{c_s^2}\right)^{1/(1-\gamma)}I_2^{-1}. \quad (12)$$

We numerically solve for R_{rcb}/R_{core} that obtains ρ_{rcb} satisfying both equations 11 and 12, using the `root_scalar` function from `SciPy optimize` package. Throughout the paper, we adopt $\gamma = 7/5$,[1] $C = -7.32$, $\alpha = 0.68$, and $\beta = 0.45$ (Rogers & Seager 2010).[2] To save computation time, we set $R_{rcb}/R_{core} = 1$ for any M_{env}/M_{core} that gives $R_{rcb}/R_{core} < 1.05$, motivated by the ~5% error in *Kepler* transit depth measurements (e.g., Fulton & Petigura 2018). This limit can be found easily by taking the limit of $R_{rcb}/R_{core} \longrightarrow 1$ and confirming numerically:

$$\left.\frac{M_{env}}{M_{core}}\right|_{min} = 4.4 \times 10^{-5}\left(\frac{M_{core}}{M_\oplus}\right)^{0.74}\left(\frac{a}{0.42\,au}\right)^{0.44}, \quad (13)$$

for $\tau_{KH} = 100$ Myrs. The numerical prefactor changes to 7×10^{-5} for $\tau_{KH} = 300$ Myrs.

The photospheric radius—the observable—is a few scale heights above R_{rcb}. Correction for the photosphere

---

[1] We note that at formation, the inner adiabat follows more closely $\gamma = 1.2$ as the energy is spent on dissociating hydrogen molecules. It is expected that γ approaches $7/5$ as the envelope cools below the dissociation temperature ~2500 K but this is yet to be verified with detailed, self-consistent calculation that tracks planets from their formation through post-disk evolution.

[2] These values are obtained by fitting to the opacities tabulated by Freedman et al. (2008), which is designed for dust-free atmospheres. In the absence of post-disk pollution by nearby small grains or giant impact, it is reasonable to consider the upper envelope to be drained out of grains (the gravitational settling timescale of a micron-sized grain is about 1 Myr).
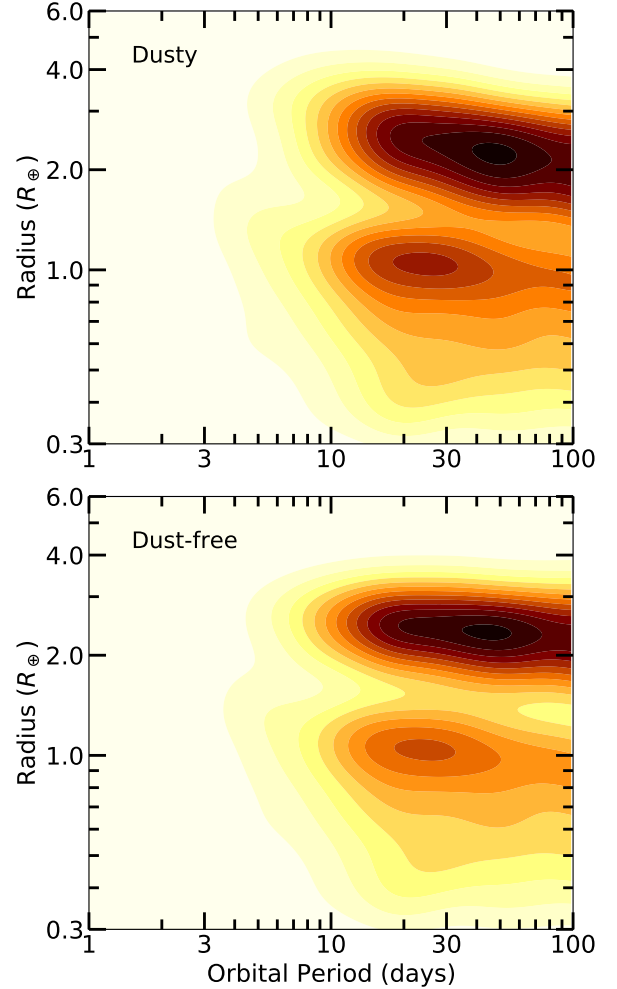

Figure 2. Primordial photometric radius vs. orbital period distribution with $f_R = 0.1$, $f_T = 2$, $\xi = 0.7$, $\rho_c = \rho_\oplus$, and $\tau_{KH} = 100$ Myrs. We smooth the model data using Gaussian kernels with Scott's Rule for bandwidth selection (`SciPy`'s `gaussian_kde` function). Gas accretion is assumed to proceed for 1 Myr in a nebula depleted by three orders of magnitude with respect to the standard solar value ($f_{dep} = 0.001$). The distinction between the two population of planets is more apparent in dust-free models. For both dusty and dust-free accretion, the rocky-to-enveloped transition shifts to smaller radii at longer orbital periods.

is made using

$$R_{phot} = R_{rcb} + \ln\left(\frac{\rho_{rcb}}{\rho_{ph}}\right)\frac{kT_{eq}}{\mu m_H g} \quad (14)$$

where $\rho_{ph} = (2/3)\mu m_H g/kT_{eq}\kappa$ is the density at the photosphere and $g \equiv GM_{core}/R_{rcb}^2$ is the surface gravity.

2.4. *Envelope mass loss*

Once the disk gas dissipates and the planets are laid bare to stellar insolation, those that are closest to the

star are expected to lose their gaseous envelopes by hydrodynamic winds, either by photoevaporation (e.g., Owen & Wu 2013) or by internal heat (e.g., Ikoma & Hori 2012; Owen & Wu 2016; Ginzburg et al. 2018). The key difference between the two mechanisms that bear on observations is the source of insolation: whereas the former depends on the high-energy flux, the latter depends on the bolometric flux. Using this difference to validate one process over another remains to be carried out. There is a discernible shift in the position of the gap towards larger radius around more massive host stars (Fulton & Petigura 2018; Cloutier & Menou 2020; Berger et al. 2020) . To reproduce this feature, photoevaporative model requires stellar-mass dependent core mass distribution (Wu 2019) whereas this is a natural prediction of Parker wind, core-powered envelope mass loss model (Gupta & Schlichting 2020). For solar-type stars, the two mechanisms predict similar location and shape of the gap in the radius-period distribution. Since the goal of this paper is to assess the likelihood of broad sub-Neptune core mass functions for a fixed mass of the host star, we limit our analysis to photoevaporative mass loss for simplicity. We discuss potential effects of varying stellar masses in Section 4.

Following Owen & Wu (2017), we evolve the envelope mass over 1 Gyrs according to the energy-limited mass loss (e.g., Lopez & Fortney 2013)

$$\dot{M}_{\text{env}} = -\eta \frac{L_{\text{HE}} R_{\text{phot}}^3}{4a^2 G(M_{\text{core}} + M_{\text{env}})} \qquad (15)$$

where $\eta = 0.1$ is the mass loss efficiency factor, and L_{HE} is the high-energy luminosity of the star (e.g., Ribas et al. 2005; Jackson et al. 2012)

$$L_{\text{HE}} = \begin{cases} 10^{-3.5} L_\odot & t < 100 \, \text{Myrs}, \\ 10^{-3.5} L_\odot \left(\frac{t}{100 \, \text{Myrs}}\right)^{-1.5} & t \geq 100 \, \text{Myrs}. \end{cases} \qquad (16)$$

Orbital periods are drawn from the empirical distribution following Petigura et al. (2018)

$$\frac{dN}{d \log P} = 0.52 \, P^{-0.1} \left[1 - \text{Exp}\left(-\left(\frac{P}{11.9 \, \text{days}} \right)^{2.4} \right) \right] \qquad (17)$$

and then converted to orbital distance assuming solar mass host star.

3. RESULTS

3.1. *Primordial Radius Valley from Late-time Gas Accretion*

We first show that late-time gas accretion alone produces a gap in the radius-period distribution (see Figure
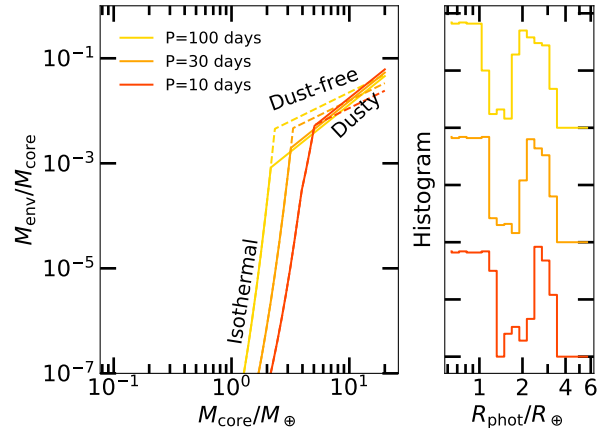

Figure 3. The primordial rocky to enveloped transition as a function of orbital period. Left: envelope mass fraction vs. core mass after 1 Myr of accretion for $f_R = 0.1$, $f_T = 2$, $\rho_c = \rho_\oplus$, and $f_{\text{dep}} = 0.001$. The maximally cooled isothermal limit truncates the gas accretion curves at $\sim$1–4$M_\oplus$. At longer orbital periods, the isothermal mass rises and so the truncation core mass shrinks. Right: histogram of photometric radii for dust-free accretion. The deep gap seen in the histogram coincides with the isothermal truncation mass shown in the left panel.

2). The amount of gaseous envelope a core can accrete drops sharply below $\sim$2$M_\oplus$ as their gas masses are limited by the maximally cooled isothermal state. The exponential dependence of this isothermal envelope mass on the core mass (equation 5) implies a bimodal distribution of envelope mass fractions and therefore a bimodal distribution of radii, for a smooth, underlying core mass function (see Figure 3).

Figure 2 demonstrates that the location of the primordial "radius valley" shifts to smaller radii farther from the star. As the disk gets colder, planet's Bondi radius increases and so the isothermal limit rises. Figure 3 illustrates this behavior where the rocky-to-enveloped transition shifts to smaller core masses at longer orbital periods. This negative slope of the valley in the radius-period space is reminiscent of that observed (Fulton et al. 2017; Van Eylen et al. 2018). We see a larger separation between the rocky and the enveloped planetary population for dust-free gas accretion. As Figure 3 shows, this difference arises from both the generally more rapid accretion and weaker dependence on core mass for dust-free envelopes.

As we will show in the next section, gas accretion needs to be dust-free in order for the primordial radius gap (and the post-evaporation gap) to align with the observation. From numerically fitting the rocky-to-enveloped transition mass (i.e., where M_{iso} (equation 5; computed numerically) crosses M_{env} (equation 4))

vs. orbital period, we find the transition mass $\propto P^{-0.31}$. Since $M_{\rm core} \propto R_{\rm core}^4$, we find the radius valley $R_{\rm valley} \propto P^{-0.08}$, in good agreement with Van Eylen et al. (2018) (within 1-σ error) and Martinez et al. (2019) (within 1.5-σ error). Following the same exercise but using temperature scaling expected from active disks $T_{\rm disk} \propto a^{-3/4}$, we obtain $R_{\rm valley} \propto P^{-0.15}$ which agrees with both Van Eylen et al. (2018) and Martinez et al. (2019) within 1.5-σ error.

3.2. *Mass Loss and Underlying Core Mass Distribution*

In the previous section, we showed how late-time gas accretion alone can produce a gap in the radius distribution and how the shape of this gap in radius-period space is in agreement with the observations. Next, we consider how envelope mass loss further molds the final radius distribution. Figure 4 demonstrates that the location of the radius valley carved out by photoevaporative mass loss is robustly situated at $\sim 1.6 R_\oplus$ regardless of the primordial population. As Owen & Wu (2017) cogently explain, gas-enveloped planets transform to bare rocky cores by photoevaporation when their envelope mass loss timescale $\lesssim 100$ Myrs, the typical saturation timescale of high-energy luminosity of host stars. For our choice of parameters, this transition occurs for $M_{\rm core} \sim 5$–$6M_\oplus$ whose core radius is ~ 1.5–$1.6 R_\oplus$ for Earth composition.

Where the initial conditions make a difference is in the depth and the width of the gap. As illustrated in Figure 4, the narrow valley and peak in the distribution of radii are more likely to appear in dust-free envelopes (blue lines) with smaller outer radius (smaller f_R) that are assembled in hotter disks (higher f_T), and built from top-heavy core mass functions (smaller ξ). Cores that are slightly less dense than the Earth ($\rho_c = 0.8\rho_\oplus$) reproduce better the observed location of the radius valley as the radii of bare cores puff up slightly pushing the location of the valley to ~ 1.7–$1.8 R_\oplus$.

The narrowness of the radius peak for dust-free envelopes as opposed to dusty envelopes can be understood from the weaker dependence of $M_{\rm env}$ on $M_{\rm core}$ (see equations 3 and 4 as well as Figure 3). For a given range of $M_{\rm core}$, the confines of possible envelope mass fractions and therefore radii are more limited.

Smaller f_R reduces the maximum $M_{\rm env}/M_{\rm core}$ and so keeps the primordial radius peak closer to the valley. Since photoevaporative mass loss effectively carves out the large radii peak and add them to the lower radii, observations are better reproduced when the initial radius valley is narrower.

In hotter disks, the isothermal maximal $M_{\rm env}/M_{\rm core}$ shrinks so that the rocky-to-enveloped transition appears at higher core masses. The result is a positive shift

in the location of the primordial radius valley. The gas accretion rate for dust-free envelopes also reduces (see equation 4) and so the sub-Neptune peak shifts closer to $\sim 2R_\oplus$, bringing the primordial distribution of radii in better agreement with the observation (see the faint blue line in the top third panel of Figure 4). Since the locations of the valley are coincident with that expected from photoevaporative mass loss, we only observe slight reduction in the peak at $\sim 2R_\oplus$ and a slight shallowing of the valley at $\sim 1.6 R_\oplus$.

We observe a loss of a peak in the radius distribution when the underlying core mass function is too bottom-heavy ($\xi = 1.3$). While we defer detailed formal fitting of models to the data for future analyses, it is already apparent that the allowed range of ξ appears tightly constrained, under the ansatz that the core mass distribution follows a power-law. It may be possible to restore the radius peak even with $\xi = 1.3$ with sufficiently high f_T but we judge $f_T > 3$ to be unlikely as it implies the disk is hot enough to melt iron at ~ 0.1 AU.

The combinations of parameters that provides the model radius distribution agreeing best with the observation are highlighted in Figure 5, corresponding to dust-free envelopes and $f_R, f_T, \xi, \rho_c/\rho_\oplus = (0.1, 2, 0.7, 0.8)$. Between the primordial and evaporated population, we see a closing of the gap at $\lesssim 30$ days as sub-Neptunes are whittled down to bare rocky objects by photoevaporation. This transformation also fills in the valley in one-dimensional radius histogram. In fact, planet population that evolved from late time gas accretion without any subsequent mass loss (right column) appears to reproduce best the observed radius valley.

The observed radius valley closes at ~ 10 days and widens towards ~ 100 days (Fulton & Petigura 2018). In photoevaporation models that assume all cores to have started with $\gtrsim 0.01\%$ by mass envelope, this triangular delta is hard to reproduce if the underlying core mass function is assumed flat (see, e.g., Owen & Wu 2013). Accounting for core mass-dependent initial envelope mass fraction alleviates the need for peaked core mass distribution as the radius gap is already carved out and photoevaporative mass loss preferentially transforms short-period sub-Neptunes into super-Earths, closing the gap inside ~ 30 days (see middle column of Figure 5).

4. DISCUSSION AND CONCLUSION

We demonstrated that the underlying core mass distribution of sub-Neptunes can be broad with substantial population of sub-Earth mass objects while still reproducing the observed gap in the radius distribution and in radius-period space. A radius gap is already in place
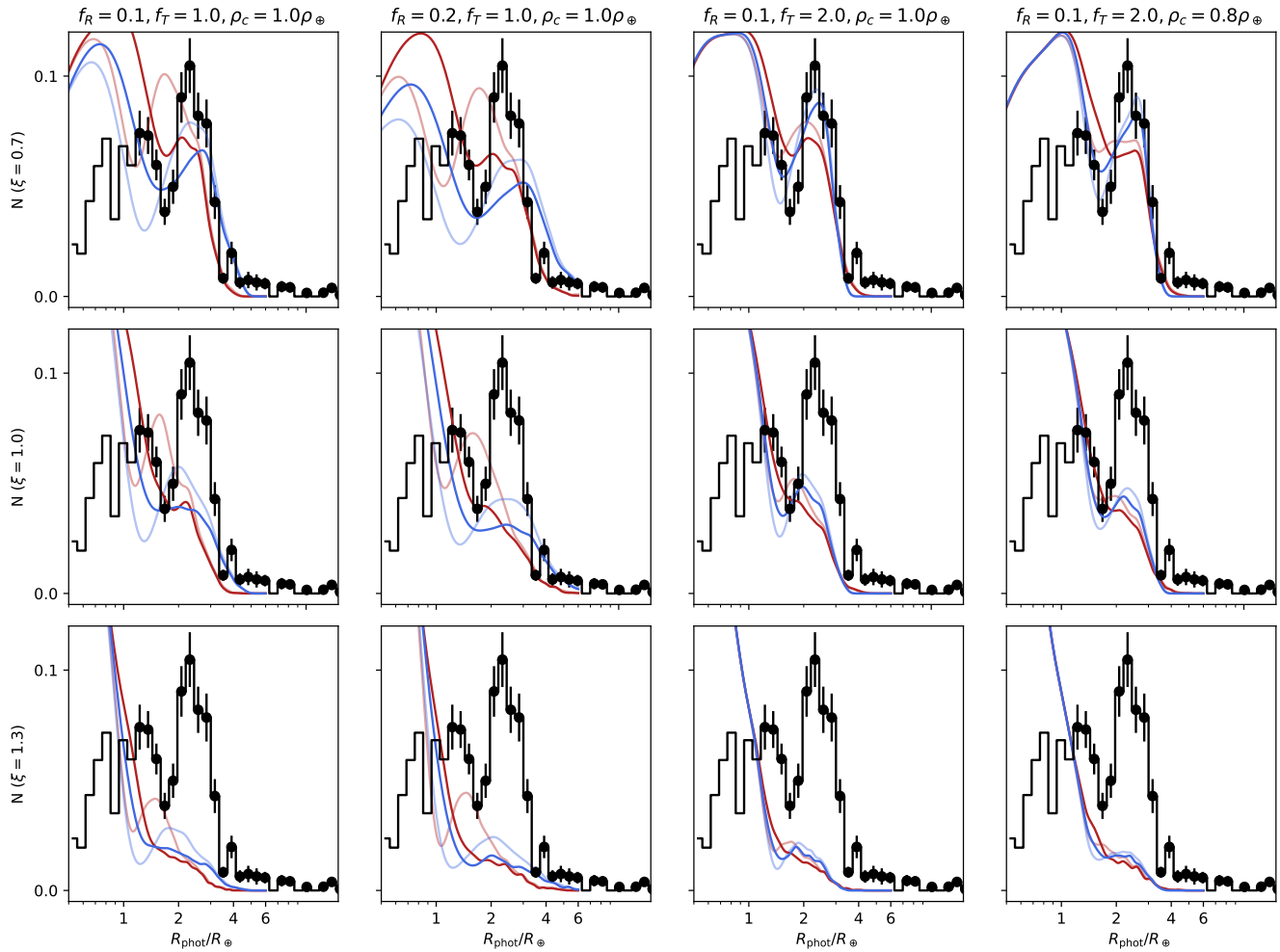
Figure 4. Distribution of planetary radii for a variety of underlying core mass distributions (ξ), truncation factor of the outer radius due to hydrodynamic effects (f_R), the disk temperature (f_T), and the core density (ρ_c). Model histograms are smoothed using Gaussian kernels with Scott's Rule for bandwidth selection (`SciPy`'s `gaussian_kde` function). Dusty and dust-free calculations are shown in red and blue, respectively, with the primordial population drawn in lighter color while the post-evaporation populations are drawn in darker color. Data from Fulton & Petigura (2018) are illustrated in black; data below $\sim 1 R_\oplus$ falls off their detection threshold and so the true sub-Earth population may be under-represented (see, e.g., Hsu et al. 2019). In general, the location of the radius valley carved out by photoevaporation is robust to varying initial conditions while the depth and the width of the valley change considerably: hotter disks narrows the gap; larger f_R broadens the overall radii distribution; fluffier cores shift the valley to larger radii; and core mass distributions that are neutral or bottom heavy are unable to reproduce the observed strong peak at $\sim 2 R_\oplus$. Among the combinations of parameters shown in this figure, dust-free envelopes with $\xi = 0.7$, $f_R = 0.1$, $f_T = 2.0$, and $\rho_c = 0.8 \rho_\oplus$ agree best with the observation.

at birth as cores lighter than ~ 1–$2 M_\oplus$ can never accrete enough gas to be observed as gas-enveloped. The maximum envelope mass given by the maximally cooled isothermal state drops exponentially with smaller core masses so that for a smooth distribution of core masses, a sharp radius dichotomy across ~ 1–$2 R_\oplus$ appears. Furthermore, this primordial radius gap shifts to smaller radii at longer orbital periods as the maximum isothermal mass rises and so the rocky-to-enveloped transition shifts to smaller cores.

Late-time formation of sub-Neptune is often attributed to producing a positive slope of the radius-period valley, based on the calculation of Lopez & Rice (2018). As these authors state, and we emphasize, their calculation is appropriate for formation in a gas-empty environment after a complete disk gas dispersal. The positive slope of the radius-period gap obtains from computing the expected core masses in a minimum mass extrasolar nebula (MMEN; Chiang & Laughlin 2013) which produces rising masses (and therefore radii) at larger orbital distances (using the updated MMEN by
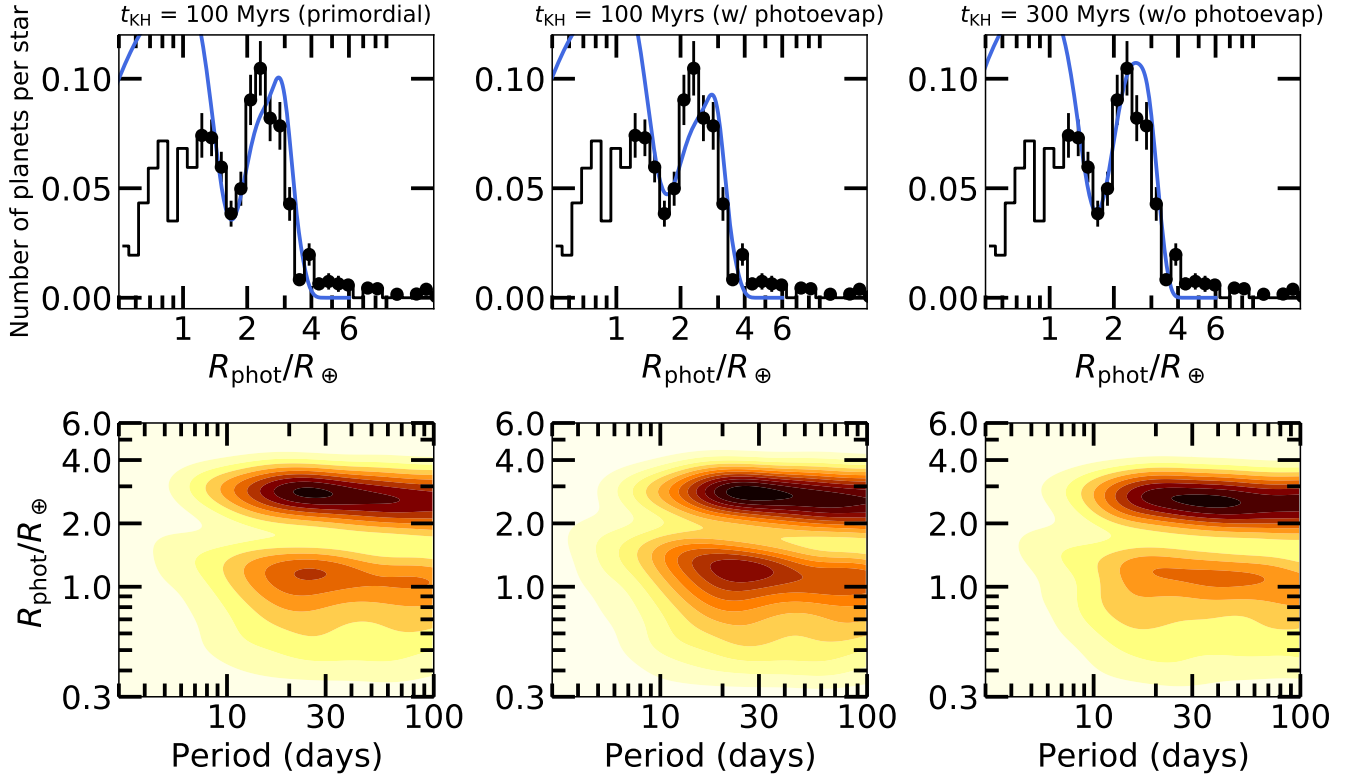
Figure 5. Radius histogram and radius-period distribution of model populations ($\xi = 0.7$, $f_T = 2.0$, $\rho_c = 0.8\rho_\oplus$, $f_R = 0.1$, $f_{\rm dep} = 0.001$) that best agree with the observations. Left: primordial population of planets that assembled in gas-poor environment. Middle: population depicted in left processed by photoevaporative mass loss over 1 Gyrs. Right: planets that assembled in gas-poor environment evolved for 1 Gyrs without any mass loss. Data from Fulton & Petigura (2018) are drawn in black. We note that data below $\sim1R_\oplus$ falls off their detection threshold and so the true sub-Earth population may be under-represented (see, e.g., Hsu et al. 2019). Photoevaporation transforms sub-Neptunes into super-Earths effectively filling in the radius gap. The shapes of both the valley and the peak in one-dimensional radius distribution are best reproduced in the evolved model without mass loss. Quantitatively, the radius valley in the pure accretion model scales with orbital period as $R_{\rm valley} \propto P^{-0.08}$, in good agreement with Van Eylen et al. (2018) (within 1-σ error) and Martinez et al. (2019) (within 1.5-σ error).

Dai et al. (2020) will produce a similar result). The slope of the valley in the radius-period space may indeed turn positive around low mass stars (Cloutier & Menou 2020; but see Wu 2019). Our premise is distinct: we consider the formation of sub-Neptunes in gas-poor but not gas-empty nebula so that gas accretion, however limited, occurs. It is formation that is late-time in terms of the evolution of disk gas but not so late that there is no gas left (e.g., inner holes of transitional disks).

Our model of late-time gas accretion best reproduces the observed location, width, and depth of the radius gap when the sub-Neptune cores follow mass functions shallower than $dN/dM_{\rm core} \propto M_{\rm core}^{-1}$ and accrete dust-free gas in hot disks.[3] The rate of accretion in dusty environment is too sensitive to core mass so that the final distribution of envelope mass fractions and therefore radii is too broad compared to that observed. The coagulation and the rain-out of dust grains may be an efficient process in sub-Neptune envelopes (Ormel 2014).

4.1. Dependence on Disk Temperature and Stellar Mass

The required disk temperatures may be uncomfortably high. We note that for accretion disks, the mid-plane temperature at ~0.1 AU can be as high as ~2000K

---

[3] We find a potentially good agreement using a bottom-heavy core mass function $dN/dM_{\rm core} \propto M_{\rm core}^{-1.1}$ for puffy cores but only in one-dimensional radius histogram. The triangular shape of the radius-period valley is challenging to reproduce with bottom-heavy core mass functions.
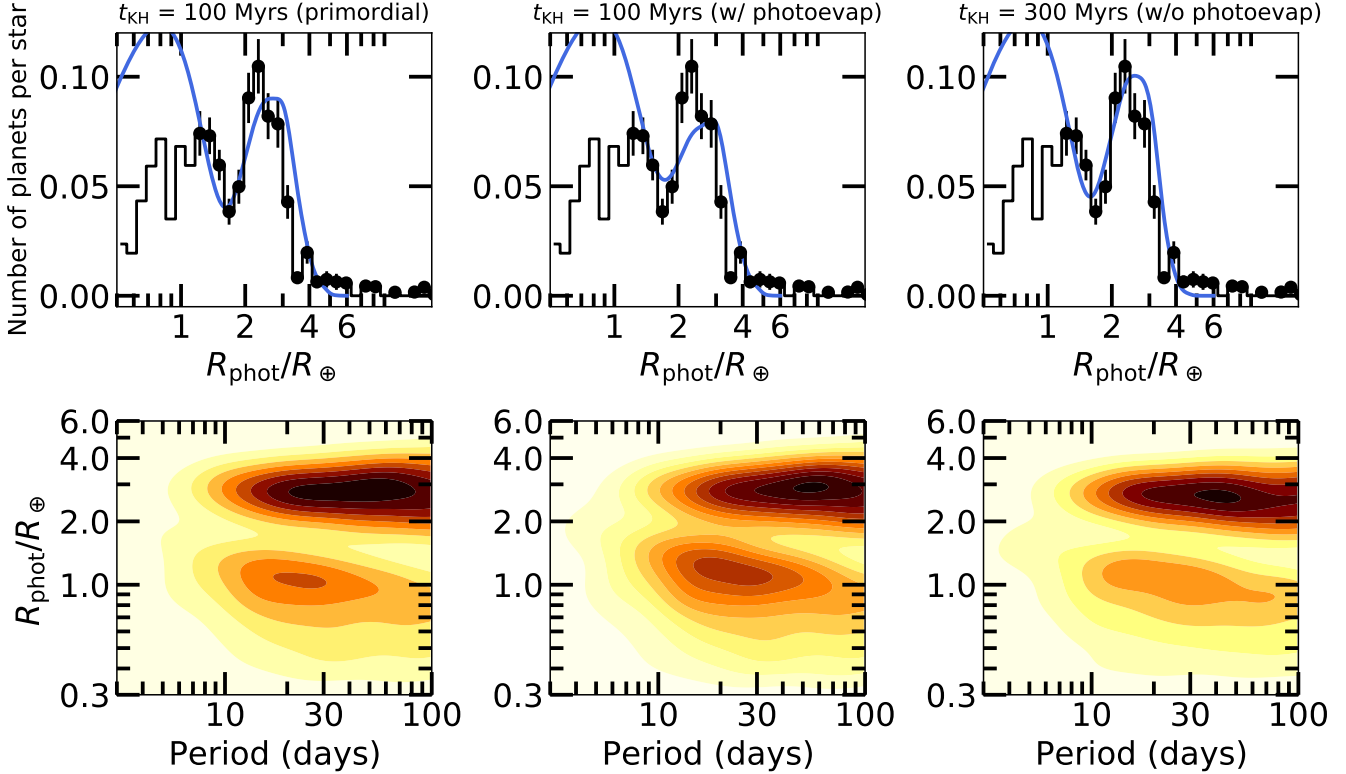
Figure 6. Same as Figure 5 except we use the disk temperature scaling that is appropriate for disks heated by viscous accretion, $T_{\rm disk} = f_T \times 1000{\rm K}(a/0.1{\rm au})^{-3/4}$. We obtain a radius valley that is steeper in the radius-period space: $R_{\rm valley} \propto P^{-0.15}$ which agrees with both Van Eylen et al. (2018) and Martinez et al. (2019) within 1.5-σ error.

(see D'Alessio et al. 1998, their Figure 3), consistent with our $f_T = 2$. D'Alessio et al. (1998) accounted for both accretional and irradiation heating where the former tends to dominate in the inner disk. The expected midplane temperature from accretion depends on the accretion rate to the power of 1/4. D'Alessio et al. (1998) adopted the typical T Tauri accretion rate $\dot{M} = 10^{-8} M_\odot \, {\rm yr}^{-1}$. With $f_\rho = 0.001$ with respect to MMEN that we adopted here, this accretion rate can be attained with Shakura-Sunyaev viscous parameter $\alpha \sim 8 \times 10^{-3}$ which is larger than what is usually inferred from studies of turbulence in protoplanetary disks such as HL tau (Pinte et al. 2016), but it is below the largest detected level of turbulence in e.g., DM Tau (Flaherty et al. 2020). For optically thick disks, the midplane temperature further enhances by a factor $\tau^{1/4}$ where τ is the vertical optical depth. D'Alessio et al. (1998) compute $\tau \sim 400$ at 0.1 AU (see their Figure 2) which can be accommodated with $f_\rho = 0.001$ assuming well-mixed dust-gas mixture within the disk (see Lee et al. 2018, their Figure 1). (This enhancement of midplane temperature by $\tau^{1/4}$ applies to passive disks as well.) Gas accretion onto planets can still proceed in dust-free manner as long as the dust grains coagulate and settle within

the planetary atmosphere (e.g., Ormel 2014). Figure 6 demonstrates that qualitative result—that late-time gas accretion alone can reproduce the radius valley at the observed location—holds when we explicitly adopt the disk temperature scaling that is appropriate for disk heated by viscous accretion (i.e., active disks).

Matching the location of the primordial radius valley with that observed requires that the sub-Neptune cores are slightly less dense, e.g., $\sim$80% of the Earth composition, in rough agreement with what is reported for short-period super-Earths by Dorn et al. (2019) and more generally by Rogers & Owen (2020). We note that some of the model parameters that produce a broad peak may be narrowed by taking into account core-envelope interaction, in particular, the dissolution of gas into the magma core (Kite et al. 2019). Assessing the effect of core-envelope mixing at formation is a subject of our ongoing work.

We note that the primordial radius valley is expected to shift towards larger sizes around higher mass stars, assuming their disks are hotter. For disks heated by stellar irradiation, $T_{\rm disk} \propto T_{\rm eff}(R_\star/a)^{1/2}$ where $T_{\rm eff} \propto M_\star^{1/7}$ is the effective temperature of the star and $R_\star \propto M_\star^{1/2}$ is the radius of the star, all evaluated for fully convective,

pre-main sequence stars (e.g., Kippenhahn et al. 2012).[4] For these passive disks, $T_{\text{disk}} \propto M_\star^{11/28}$. From numerical fitting, we find the rocky-to-gas-enveloped transition core mass $M_{\text{c,trans}} \propto T_{\text{disk}}^{1.09}$ and $R_c \propto M_c^{1/4}$ so the radius valley $R_{\text{val}} \propto M_\star^{0.11}$. For disks heated by accretion, $T_{\text{disk}} \propto (M_\star \dot{M}/R_\star^3)^{1/4}(a/R_\star)^{-3/4}$ (Clarke & Carswell 2007). Taking $\dot{M} \propto M_\star^{1.95}$ (Calvet et al. 2004), we find $T_{\text{disk}} \propto M_\star^{0.7}$. Again, from numerical fitting but for active disks, $M_{\text{c,trans}} \propto T_{\text{disk}}^{2.10}$ and so $R_{\text{val}} \propto M_\star^{0.37}$. Both estimates are within the 1-σ error bar estimate from Gaia-Kepler catalog by Berger et al. (2020).

We conclude this section by noting that computing disk temperature depends on uncertain factors including dust grain size distribution that can vary both radially and vertically. The disk temperatures we adopted in this paper are in the realm of possibility but more accurate comparison with observations will require better understanding of the thermal structure of the protoplanetary disks and their dependence on the host stellar mass.

4.2. *Primordial vs. Mass Loss*

Late-time gas accretion alone can carve out a valley in radius-period distribution of exoplanets. In fact, in many of the cases we explore, the agreement with the data becomes worse after taking into account photoevaporative mass loss, as the radius gap fills up. Intriguingly, David et al. (2020) report the radius gap appears more filled in around stars older than $\sim$2 Gyrs, potentially consistent with our results as long as the dominant mass loss process operates over 1–2 Gyrs which can be either photoevaporation (e.g., King & Wheatley 2020) or core-powered mass loss (e.g., Ginzburg et al. 2018) (or both). We note however that Berger et al. (2020) report no discernible change in the depth of the gap across stellar ages of $\sim$1 Gyr. What the two studies have in common is that the relative number fraction of super-Earth rises around older stars, suggesting long-term mass loss processes are likely in effect.

There remain uncertainties in the exact magnitude of the mass loss for both photoevaporation and core-powered mass loss models. In the picture of photoevaporation, the unknown strength of planetary magnetic fields can shield against high-energy stellar photons (Owen & Adams 2019). Furthermore, there is an order of magnitude variation in the magnitude and time evolution of stellar EUV and X-ray luminosity (Tu et al. 2015). In the picture of core-powered envelope mass loss, the amount of gas mass that can be lost via wind depends on the structure of the outer envelope subject to uncertain opacity sources. Even if the cores hold enough thermal energy to unbind the entire envelope, the timescale of heat transfer depends on the unknown viscosity and Prandtl number of the magma/rocky core (e.g., Stamenković et al. 2012; Garaud 2018; Fuentes & Cumming 2020). Further advances in both theory and observations should iron out these uncertainties.

---

[4] Mass-radius relationship for fully convective pre-main sequence star can be obtained by evaluating time evolution of radius with luminosity given by convection: $R_\star \propto t^{-1/3} M_\star^{1/2}$.

REFERENCES

Ali-Dib, M., Cumming, A., & Lin, D. N. C. 2020, MNRAS, 494, 2440, doi: 10.1093/mnras/staa914

Berger, T. A., Huber, D., Gaidos, E., van Saders, J. L., & Weiss, L. M. 2020, arXiv e-prints, arXiv:2005.14671. https://arxiv.org/abs/2005.14671

Burke, C. J., Christiansen, J. L., Mullally, F., et al. 2015, ApJ, 809, 8, doi: 10.1088/0004-637X/809/1/8

Calvet, N., Muzerolle, J., Briceño, C., et al. 2004, AJ, 128, 1294, doi: 10.1086/422733

Chiang, E., & Laughlin, G. 2013, MNRAS, 431, 3444, doi: 10.1093/mnras/stt424

Choksi, N., & Chiang, E. 2020, MNRAS, 495, 4192, doi: 10.1093/mnras/staa1421

Clarke, C., & Carswell, B. 2007, Principles of Astrophysical Fluid Dynamics

Cloutier, R., & Menou, K. 2020, AJ, 159, 211, doi: 10.3847/1538-3881/ab8237

Dai, F., Winn, J. N., Schlaufman, K., et al. 2020, AJ, 159, 247, doi: 10.3847/1538-3881/ab88b8

D'Alessio, P., Cantö, J., Calvet, N., & Lizano, S. 1998, ApJ, 500, 411, doi: 10.1086/305702

David, T. J., Contardo, G., Sandoval, A., et al. 2020, arXiv e-prints, arXiv:2011.09894. https://arxiv.org/abs/2011.09894

Dawson, R. I., Chiang, E., & Lee, E. J. 2015, MNRAS, 453, 1471, doi: 10.1093/mnras/stv1639

Dorn, C., Harrison, J. H. D., Bonsor, A., & Hands, T. O. 2019, MNRAS, 484, 712, doi: 10.1093/mnras/sty3435

Flaherty, K., Hughes, A. M., Simon, J. B., et al. 2020, ApJ, 895, 109, doi: 10.3847/1538-4357/ab8cc5

Freedman, R. S., Marley, M. S., & Lodders, K. 2008, ApJS, 174, 504, doi: 10.1086/521793

Fressin, F., Torres, G., Charbonneau, D., et al. 2013, ApJ, 766, 81, doi: 10.1088/0004-637X/766/2/81

Fuentes, J. R., & Cumming, A. 2020, arXiv e-prints, arXiv:2007.04265. https://arxiv.org/abs/2007.04265

Fulton, B. J., & Petigura, E. A. 2018, AJ, 156, 264, doi: 10.3847/1538-3881/aae828

Fulton, B. J., Petigura, E. A., Howard, A. W., et al. 2017, AJ, 154, 109, doi: 10.3847/1538-3881/aa80eb

Fung, J., Zhu, Z., & Chiang, E. 2019, ApJ, 887, 152, doi: 10.3847/1538-4357/ab53da

Garaud, P. 2018, Annual Review of Fluid Mechanics, 50, 275, doi: 10.1146/annurev-fluid-122316-045234

Ginzburg, S., Schlichting, H. E., & Sari, R. 2016, ApJ, 825, 29, doi: 10.3847/0004-637X/825/1/29

—. 2018, MNRAS, 476, 759, doi: 10.1093/mnras/sty290

Gupta, A., & Schlichting, H. E. 2020, MNRAS, 493, 792, doi: 10.1093/mnras/staa315

Hadden, S., & Lithwick, Y. 2014, ApJ, 787, 80, doi: 10.1088/0004-637X/787/1/80

Hsu, D. C., Ford, E. B., Ragozzine, D., & Ashby, K. 2019, AJ, 158, 109, doi: 10.3847/1538-3881/ab31ab

Ikoma, M., & Hori, Y. 2012, ApJ, 753, 66, doi: 10.1088/0004-637X/753/1/66

Jackson, A. P., Davis, T. A., & Wheatley, P. J. 2012, MNRAS, 422, 2024, doi: 10.1111/j.1365-2966.2012.20657.x

King, G. W., & Wheatley, P. J. 2020, arXiv e-prints, arXiv:2007.13731. https://arxiv.org/abs/2007.13731

Kippenhahn, R., Weigert, A., & Weiss, A. 2012, Stellar Structure and Evolution, doi: 10.1007/978-3-642-30304-3

Kite, E. S., Fegley, Bruce, J., Schaefer, L., & Ford, E. B. 2019, ApJL, 887, L33, doi: 10.3847/2041-8213/ab59d9

Lambrechts, M., & Lega, E. 2017, A&A, 606, A146, doi: 10.1051/0004-6361/201731014

Lee, E. J., & Chiang, E. 2015, ApJ, 811, 41, doi: 10.1088/0004-637X/811/1/41

—. 2016, ApJ, 817, 90, doi: 10.3847/0004-637X/817/2/90

Lee, E. J., Chiang, E., & Ferguson, J. W. 2018, MNRAS, 476, 2199, doi: 10.1093/mnras/sty389

Lee, E. J., Chiang, E., & Ormel, C. W. 2014, ApJ, 797, 95, doi: 10.1088/0004-637X/797/2/95

Lopez, E. D., & Fortney, J. J. 2013, ApJ, 776, 2, doi: 10.1088/0004-637X/776/1/2

—. 2014, ApJ, 792, 1, doi: 10.1088/0004-637X/792/1/1

Lopez, E. D., & Rice, K. 2018, MNRAS, 479, 5303, doi: 10.1093/mnras/sty1707

Malhotra, R. 2015, ApJ, 808, 71, doi: 10.1088/0004-637X/808/1/71

Marcy, G. W., Isaacson, H., Howard, A. W., et al. 2014, ApJS, 210, 20, doi: 10.1088/0067-0049/210/2/20

Martinez, C. F., Cunha, K., Ghezzi, L., & Smith, V. V. 2019, ApJ, 875, 29, doi: 10.3847/1538-4357/ab0d93

Ormel, C. W. 2014, ApJL, 789, L18, doi: 10.1088/2041-8205/789/1/L18

Owen, J. E., & Adams, F. C. 2019, MNRAS, 490, 15, doi: 10.1093/mnras/stz2601

Owen, J. E., & Wu, Y. 2013, ApJ, 775, 105, doi: 10.1088/0004-637X/775/2/105

—. 2016, ApJ, 817, 107, doi: 10.3847/0004-637X/817/2/107

—. 2017, ApJ, 847, 29, doi: 10.3847/1538-4357/aa890a

Petigura, E. A., Howard, A. W., & Marcy, G. W. 2013, Proceedings of the National Academy of Science, 110, 19273, doi: 10.1073/pnas.1319909110

Petigura, E. A., Marcy, G. W., Winn, J. N., et al. 2018, AJ, 155, 89, doi: 10.3847/1538-3881/aaa54c

Pinte, C., Dent, W. R. F., Ménard, F., et al. 2016, ApJ, 816, 25, doi: 10.3847/0004-637X/816/1/25

Pollack, J. B., Hubickyj, O., Bodenheimer, P., et al. 1996, Icarus, 124, 62, doi: 10.1006/icar.1996.0190

Ribas, I., Guinan, E. F., Güdel, M., & Audard, M. 2005, ApJ, 622, 680, doi: 10.1086/427977

Rogers, J. G., & Owen, J. E. 2020, arXiv e-prints, arXiv:2007.11006. https://arxiv.org/abs/2007.11006

Rogers, L. A., & Seager, S. 2010, ApJ, 712, 974, doi: 10.1088/0004-637X/712/2/974

Stamenković, V., Noack, L., Breuer, D., & Spohn, T. 2012, ApJ, 748, 41, doi: 10.1088/0004-637X/748/1/41

Tu, L., Johnstone, C. P., Güdel, M., & Lammer, H. 2015, A&A, 577, L3, doi: 10.1051/0004-6361/201526146

Valencia, D., O'Connell, R. J., & Sasselov, D. 2006, Icarus, 181, 545, doi: 10.1016/j.icarus.2005.11.021

Van Eylen, V., Agentoft, C., Lundkvist, M. S., et al. 2018, MNRAS, 479, 4786, doi: 10.1093/mnras/sty1783

Weiss, L. M., & Marcy, G. W. 2014, ApJL, 783, L6, doi: 10.1088/2041-8205/783/1/L6

Wu, Y. 2019, ApJ, 874, 91, doi: 10.3847/1538-4357/ab06f8

Wu, Y., & Lithwick, Y. 2013, ApJ, 772, 74, doi: 10.1088/0004-637X/772/1/74